

# CM-Bench: A Comprehensive Cross-Modal Feature Matching Benchmark Bridging Visible and Infrared Images

Liangzheng Sun<sup>1</sup>, Mengfan He<sup>2</sup>, Xingyu Shao<sup>2</sup>, Binbin Li<sup>1</sup>, Zhiqiang Yan<sup>1</sup>, Chunyu Li<sup>2</sup>, Ziyang Meng<sup>2</sup>, Fei Xing<sup>2</sup>

**Abstract**—Infrared-visible (IR-VIS) feature matching plays an essential role in cross-modality visual localization, navigation and perception. Along with the rapid development of deep learning techniques, a number of representative image matching methods have been proposed. However, cross-modal feature matching is still a challenging task due to the significant appearance difference. A significant gap for cross-modal feature matching research lies in the absence of standardized benchmarks and metrics for evaluations. In this paper, we introduce a comprehensive cross-modal feature matching benchmark, CM-Bench, which encompasses 30 feature matching algorithms across diverse cross-modal datasets. Specifically, state-of-the-art traditional and deep learning-based methods are first summarized and categorized into sparse, semi-dense, and dense methods. These methods are evaluated by different tasks including homography estimation, relative pose estimation, and feature-matching-based geo-localization. In addition, we introduce a classification-network-based adaptive preprocessing front-end that automatically selects suitable enhancement strategies before matching. We also present a novel infrared-satellite cross-modal dataset with manually annotated ground-truth correspondences for practical geo-localization evaluation. The dataset and resource will be available at: <https://github.com/SLZ98/CM-Bench>.

## I. INTRODUCTION

Infrared (IR) and visible (VIS) image sensors are widely used in numerous realistic applications, such as security monitoring [1], remote sensing [2] and autonomous vehicles [3]. They provide different but complementary modal information, and therefore leveraging cross-modal information is essential for achieving a robust system. In particular, the integration of cross-modal sensing information requires reliable data association through feature matching, while existing feature matching methods primarily focus on algorithm design tailored for visible image sensors. It remains unclear whether these methods are still feasible for cross-modal feature matching task. Specifically, traditional feature

Liangzheng Sun and Mengfan He contributed equally to this work. Corresponding author: Ziyang Meng.

<sup>1</sup>School of Instrument Science and Opto-Electronics Engineering, Beijing Information Science and Technology University, Beijing 100192, China 2023030031@bistu.edu.cn; 2024020382@bistu.edu.cn; 2024020267@bistu.edu.cn

<sup>2</sup>Department of Precision Instrument, Tsinghua University, Beijing 100084, China hmf21@mails.tsinghua.edu.cn; shao-xy21@mails.tsinghua.edu.cn; lcyfly1@163.com; ziyangmeng@mail.tsinghua.edu.cn; xingfei@mail.tsinghua.edu.cn

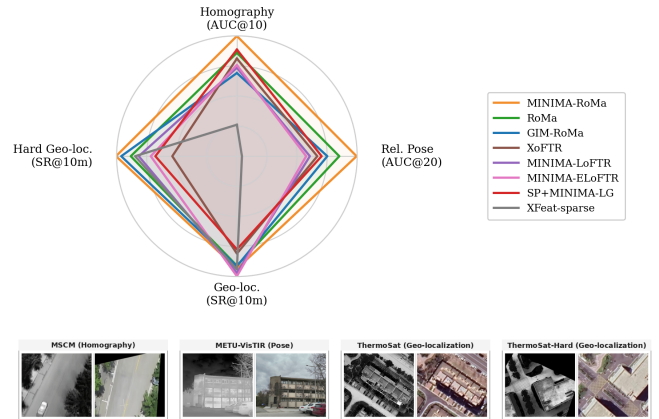


Fig. 1. Overview of eight representative matchers across four benchmark tasks, together with representative samples from the corresponding evaluation settings.

matching algorithms are prone to fail because of their reliance on intensity or texture similarity. On the other hand, deep-learning methods have demonstrated strong capabilities in learning discriminative features. However, their generalization to cross-modal tasks remains largely under-explored. Additionally, algorithms specially designed for cross-modal matching are often evaluated in a constrained dataset and lack of fully comparison. To the best of our knowledge, the systematic evaluation for cross-modal feature matching has not been explored, from a comprehensive collection of datasets to consistent evaluation metrics.

Another major challenge in advancing IR-VIS feature matching lies in the limited availability of high-quality datasets tailored for cross-modal tasks. Existing cross-modal datasets are often either too small or lack diversity in environmental settings and viewpoints to support effective evaluation. Furthermore, in addition to cross-modal feature matching technique, the image preprocessing are also promising engineering solutions to improve cross-modal feature matching performance, including contrast enhancement and edge feature extraction.

In this work, we present the first comprehensive cross-modal feature matching benchmark, named **CM-Bench**, which contains 30 feature matching algorithm evaluations in total, including traditional handcrafted features (e.g., SIFT [4], RIFT [5]), advanced deep learning-based methods (e.g. SuperPoint [6], ALIKED [7]), and methods specifically designed for cross-modal matching (e.g. XoFTR [8], MINIMA [9]). Unlike the existing benchmarks designed for the RGB-

only feature matching works [10]–[12], CM-Bench presents a clarified evaluation for the cross-modal matching task. The proposed benchmark is based on utilizing a large number of publicly available datasets and self-collected data for comprehensive evaluation. Fig. 1 provides an overview of performance comparisons among state-of-the-art methods across different evaluation tasks in our benchmark. The contributions are summarized as follows:

- We propose **CM-Bench**, a comprehensive comparison of **30** feature matching algorithms across **10** diverse cross-modal datasets. The evaluated algorithms include various types of methods, spanning from classic hand-crafted features to the state-of-the-art deep learning models. The selected datasets capture a variety of environments, sensor settings, and collection conditions to reflect realistic challenges.
- We present quantitative and qualitative evaluations on algorithm performance, utilizing several effective metrics. Furthermore, we introduce a classification-network-based adaptive preprocessing front-end, which automatically selects suitable enhancement strategies for different image pairs before matching.
- We release a new cross-modal dataset between infrared and satellite images, termed the Aerial Thermal–Satellite Localization Dataset (ThermoSat). The infrared images and corresponding satellite images are manually calibrated and annotated with ground-truth points. The current benchmark uses 832 annotated pairs captured by a DJI Matrice 4T platform, covering representative agricultural and urban scenes.

## II. RELATED WORK

### A. RGB-Only Image Feature Matching

Feature matching is a fundamental problem in computer vision, and many methods have been proposed for RGB-only images. These methods can be categorized into three classes based on the matching granularity: sparse keypoint-based matching, semi-dense correspondence methods, and dense correspondence techniques, which respectively focus on distinctive keypoints, larger image regions, and pixel-level correspondence.

1) *Sparse Keypoint-Based Matching*: Traditional hand-crafted methods, such as SIFT [4], ORB [13], and SURF [14], are developed for single-modal feature matching, but they often struggle in IR-VIS tasks because the assumption of consistent intensity patterns does not hold across modalities. Learning-based features such as SuperPoint [6], ALIKED [7], and R2D2 [15], together with refinement techniques such as SuperGlue [16], LightGlue [17], and Patch2Pix [18], substantially improve single-modality matching performance.

2) *Semi-Dense Correspondence*: One of the most popular approaches of semi-dense methods is LoFTR [19], which directly predicts dense correspondences between pixels without keypoint detection. Following this idea, Efficient LoFTR [20] optimizes the previous pipeline for optimal computational efficiency without performance loss. Other methods,

including ASpanFormer [21] and MatchFormer [22], extend transformer-based architectures to refine matching through hierarchical attention mechanisms and cross-scale learning.

3) *Dense Correspondence*: DKM [23] and GIM-DKM [24] are two representative dense correspondence solutions that capture detailed global relationships and align entire images based on global feature properties. Other dense matching algorithms, such as RoMa [25] and RoMa v2 [26], focus on geometric consistency to provide robust dense correspondence across different scales. On the other hand, DUS3R [27] and MAST3R [28] integrate spatial and structural constraints by directly predicting geometric relationships under viewpoint changes, although dense matching methods are often computationally demanding.

### B. Cross-Modal Feature Matching

Algorithms for RGB cameras may not excel in cross-modal matching due to generalization limits, prompting the development of task-specific cross-modal matching algorithms. A representative handcrafted cross-modal feature is RIFT [5], which utilizes multi-scale gradient orientations to ensure invariance to radiation changes. XoFTR [8] is a prominent semi-dense algorithm designed specifically for addressing modality shifts by generating pseudo infrared images during training, while MINIMA [9] uses generative models to synthesize infrared data for fine-tuning.

## III. METHODOLOGY

### A. Cross-Modal Feature Matching and Datasets

The modalities between infrared and visible exhibit substantial appearance differences, including variations in texture, contrast, edge responses and spectrum. These characteristics often cause traditional feature matching algorithms designed for single-modality scenarios to perform poorly. This study establishes a comprehensive evaluation framework to systematically assess the performance of various feature matching algorithms in IR-VIS cross-modal scenarios.

Our evaluation framework utilizes three benchmark groups. First, for homography estimation, we use the Multi-Source Cross-Modal dataset (MSCM), containing 7,083 pixel-aligned infrared-visible image pairs from eight existing datasets: (1) VisDrone, providing diverse aerial urban scenes captured from drone platforms; (2) DUT-VTUAV [29], containing diverse environments and weather conditions; (3) AVIID, providing aerial infrared-visible imagery for UAV scenarios; (4) LLVIP [30], capturing low-light urban scenes; (5) M3FD [31], covering multiple weather conditions across various scenes; (6) MSRS [32], containing multi-spectral road scenes; (7) KAIST [33], focusing on urban environments; and (8) FLIR [34], containing thermal and RGB urban street scenes.

Second, for relative pose estimation evaluation, we utilize the METU-VisTIR dataset with relative pose ground truth for building scenes. Third, we contribute our self-collected Aerial Thermal–Satellite Localization Dataset (ThermoSat), containing 832 manually annotated infrared-satellite image pairs captured by a DJI Matrice 4T platform for practical

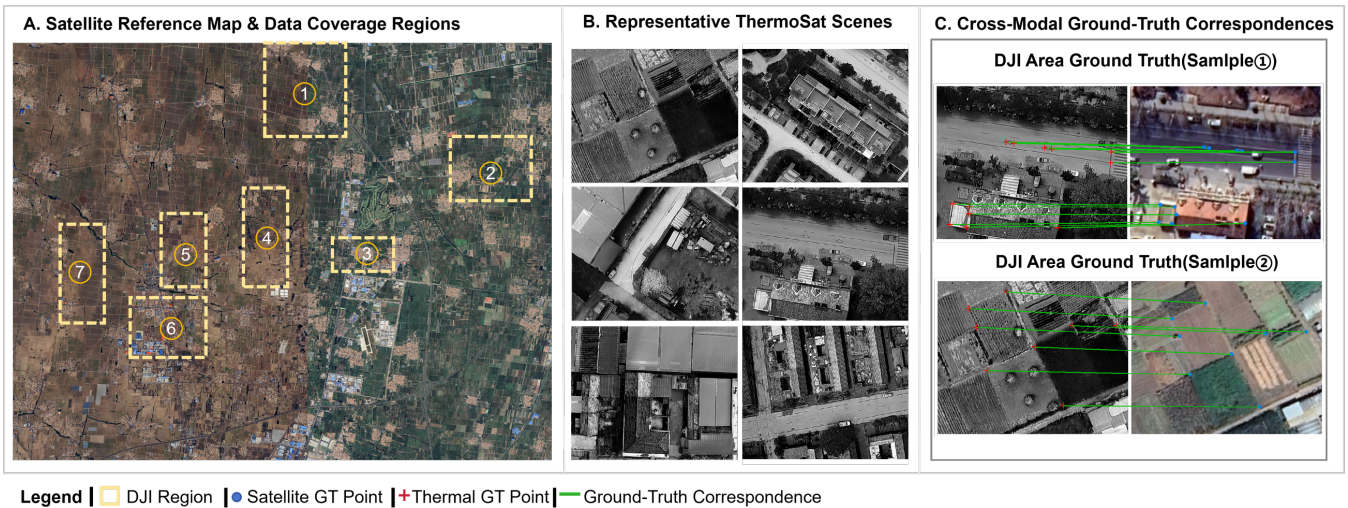


Fig. 2. Overview of the proposed ThermoSat dataset. (A) Collection area overview with seven representative thermal-to-satellite localization regions. (B) Representative ThermoSat scenes. (C) Cross-modal ground-truth correspondences, where blue dots denote satellite ground-truth points, red crosses denote thermal ground-truth points, and green lines denote ground-truth correspondences.

geo-localization evaluation. The thermal images are acquired at a resolution of  $1280 \times 1024$ . The selected ThermoSat sequences provide a cumulative trajectory length of approximately 41.56 km, with a total local coverage of approximately  $35.86 \text{ km}^2$  across the seven surveyed regions. Representative collection areas, thermal scenes, and manually annotated cross-modal correspondences are shown in Fig. 2.

Our framework evaluates 30 algorithms across four key tasks: (1) Homography Estimation; (2) Relative Pose Estimation; (3) Geo-localization; and (4) Hard Geo-localization:

- **Homography Estimation:** Testing algorithms on the MSCM dataset with random homography transformations to evaluate cross-modal geometric robustness.
- **Relative Pose Estimation:** Using datasets with true camera poses like METU\_VisTIR to test the algorithms' performance in 3D scene reconstruction and pose recovery.
- **Geo-localization:** Evaluating practical thermal-to-satellite geo-localization using our self-collected Aerial Thermal-Satellite Localization Dataset (ThermoSat).
- **Hard Geo-localization:** Evaluating the same ThermoSat benchmark under a harder protocol constructed from the corresponding ThermoSat sequences by introducing additional flight-induced viewpoint perturbations, including attitude-angle changes and altitude variations, while keeping the underlying thermal-to-satellite localization scenes unchanged.

This four-task evaluation framework systematically assesses IR-VIS matching algorithms across a complexity spectrum—from geometric robustness (Homography Estimation) and 3D scene understanding (Relative Pose Estimation) to geo-localization (Geo-localization).

### B. Adaptive Preprocessing Front-end

Besides benchmarking the matching algorithms themselves, we further introduce an adaptive preprocessing front-

end for IR-VIS image pairs. The motivation is that no single preprocessing strategy is consistently optimal for all cross-modal image pairs. Different scenes exhibit different modality gaps in contrast, texture, and structural saliency, while different matching algorithms also respond differently to enhanced inputs. Therefore, a fixed preprocessing branch may improve weak-texture or low-contrast pairs, but it can also reduce performance on image pairs that are already matchable by altering useful intensity patterns or structural details. The overall pipeline is illustrated in Fig. 3.

To address this issue, we cast preprocessing selection as a lightweight image-pair classification problem. Given an infrared-visible image pair, we first resize both images to  $224 \times 224$  and feed them into a classification network built on a MobileNetV4-Conv-Small backbone. The backbone extracts one global feature vector for each image, denoted as  $f_{ir}$  and  $f_{vis}$ . The pair representation is then constructed by concatenating the two original features, their absolute difference  $|f_{ir} - f_{vis}|$ , and their element-wise product  $f_{ir} \odot f_{vis}$ . In this way, the fused descriptor jointly encodes single-image appearance cues, cross-modal discrepancies, and shared structural responses. A lightweight classifier then predicts the most suitable preprocessing branch for the current image pair.

The candidate branches are designed to provide complementary properties. The none branch preserves the original image appearance and avoids unnecessary distortion of radiometric and texture information. The unsharp branch strengthens local edges and fine details. The Scharr-gradient with local contrast normalization branch emphasizes gradient structure while suppressing local intensity differences across modalities. The morphological-gradient branch highlights object boundaries and region contours. To train the classifier, we use automatically generated supervision rather than manual branch annotations. Specifically, for each training image pair, we exhaustively evaluate the candidate branches and

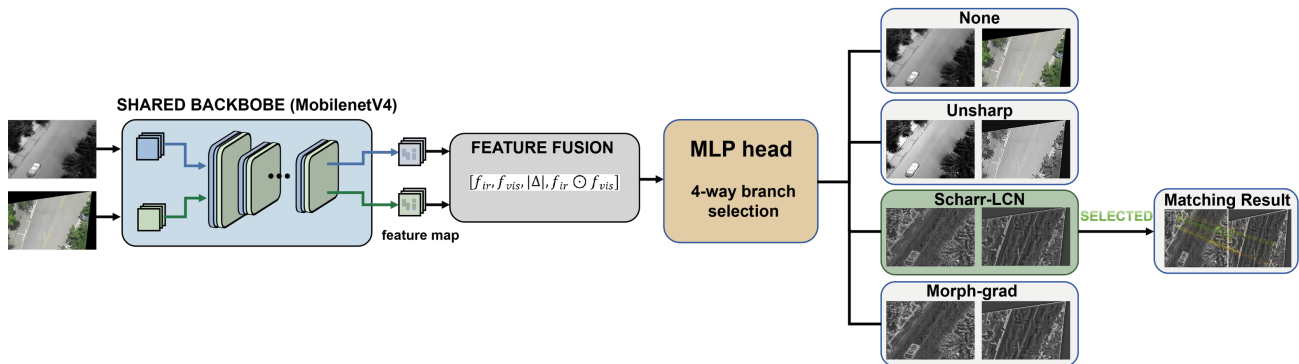


Fig. 3. Overview of the proposed adaptive preprocessing front-end. A lightweight MobileNetV4-based classifier predicts the most suitable preprocessing branch for each IR-VIS image pair before feature matching.

TABLE I

HOMOGRAPHY ESTIMATION RESULTS ON MSCM. SUCCESS RATE DENOTES THE RATIO OF VALID HOMOGRAPHY EVALUATIONS OVER 2000 TEST PAIRS, AND FAILED PAIRS ARE CALCULATED AS ZERO WHEN COMPUTING AUC.

Category	Method	Success Rate	AUC@5	AUC@10	AUC@20
Sparse	SuperPoint+MINIMA-LG	0.987	<b>0.151</b>	<b>0.452</b>	<b>0.689</b>
	SuperPoint+SuperGlue	0.971	0.114	0.358	0.559
	SuperPoint+LightGlue	0.978	0.095	0.323	0.523
	ALIKED+LightGlue	0.926	0.072	0.246	0.414
	SuperPoint+MNN	<b>1.000</b>	0.053	0.213	0.376
	DeDoDe	<b>1.000</b>	0.065	0.210	0.336
	MIFNet(XFeat)	0.931	0.043	0.187	0.387
	XFeat+LightGlue	0.883	0.033	0.151	0.297
	D2Net	<b>1.000</b>	0.030	0.151	0.326
	XFeat(sparse)	<b>1.000</b>	0.029	0.133	0.277
	RoRD	<b>1.000</b>	0.024	0.126	0.261
	R2D2	0.997	0.022	0.088	0.155
	SIFT	<b>1.000</b>	0.018	0.066	0.107
	RIFT	0.988	0.004	0.024	0.068
Semi-Dense	XoFTR	<b>1.000</b>	<b>0.136</b>	<b>0.414</b>	<b>0.640</b>
	MINIMA(ELoFTR)	0.996	0.111	0.386	0.634
	MINIMA(LoFTR)	<b>1.000</b>	0.113	0.375	0.620
	MINIMA(XoFTR)	0.935	0.126	0.366	0.573
	ELoFTR	<b>1.000</b>	0.100	0.336	0.551
	ASpanFormer	<b>1.000</b>	0.091	0.323	0.539
	TopicFM	<b>1.000</b>	0.089	0.299	0.509
	LoFTR	<b>1.000</b>	0.084	0.295	0.499
Dense	MINIMA(RoMa)	<b>1.000</b>	<b>0.198</b>	<b>0.509</b>	<b>0.733</b>
	RoMa	<b>1.000</b>	0.151	0.438	0.672
	GIM(RoMa)	<b>1.000</b>	0.114	0.353	0.580
	RoMa v2	<b>1.000</b>	0.075	0.257	0.467
	GIM(DKM)	<b>1.000</b>	0.076	0.245	0.405
	MASt3R	0.995	0.065	0.232	0.410
	XFeat(dense)	0.999	0.026	0.145	0.308
	DKM	<b>1.000</b>	0.003	0.025	0.069

assign as the target label the branch that produces the largest number of geometric inliers after matching and RANSAC verification [35]. The gate network is then optimized as a four-class classifier with the standard cross-entropy loss. The selected branch is finally applied to both modalities before feature extraction and matching, allowing the front-end to adapt to different scene structures and cross-modal appearance gaps. In its current implementation, the gate network contains 7.74M parameters and introduces approximately 21.1 ms runtime overhead per image pair on a single RTX 4090 GPU at an input resolution of  $224 \times 224$ .

### C. Evaluation Methodology and Metrics

Our evaluation framework employs multiple quantitative metrics to comprehensively assess the performance of differ-

ent feature matching algorithms in infrared-visible (IR-VIS) cross-modal scenarios, focusing on four main as follows.

1) *Homography Estimation Metrics and Relative Pose Estimation Metrics*: To evaluate the performance of feature matching methods in geometric tasks, we conduct homography estimation experiments on the MSCM dataset using synthetic geometric transformations. A single random homography transformation is applied to each image pair to provide the corresponding ground-truth homography for evaluation. The transformation parameters are sampled with scale ranging from 0.65 to 1.35, rotation ranging from  $-25^\circ$  to  $25^\circ$ , perspective jitter ranging from  $-0.23$  to  $0.23$ , and translation ranging from  $-0.17$  to  $0.17$  relative to the image width and height, while maintaining at least 60% valid overlap. We evaluate homography estimation accuracy using the Area Under the Curve (AUC) with thresholds of 5, 10 and 20 pixels, denoted as AUC@5, AUC@10, and AUC@20, where failed pairs contribute to zero. For relative pose estimation, we also report AUC values at thresholds of  $5^\circ$ ,  $10^\circ$ , and  $20^\circ$ . To reduce scene imbalance, we first compute scene-level pose AUC values, then average the scenes within the *cloudy-cloudy* and *cloudy-sunny* splits, and finally combine the two split-level AUCs according to the number of scenes in each split:

$$\text{AUC@}\tau = \frac{1}{\tau} \int_0^\tau \text{Recall}(\epsilon) d\epsilon \quad (1)$$

where  $\tau$  represents the threshold value (measured in pixels for homography estimation or in degrees for relative pose estimation), and  $\text{Recall}(\epsilon)$  is the proportion of errors below  $\epsilon$ . For both homography estimation and relative pose estimation, higher AUC values indicate better geometric accuracy and robustness under more stringent evaluation thresholds.

2) *Geo-localization Metrics*: For geo-localization and hard geo-localization, we measure localization accuracy in meters using the manually annotated ground-truth correspondences on the geo-referenced image. For each image pair, let  $e_i$  denote the localization error in meters, computed as the root-mean-square distance between the projected points and the corresponding ground-truth points. Based on these per-pair errors, we report the median localization error over successfully evaluated pairs, denoted as  $\text{MedErr}_m$ , and the

TABLE II

RELATIVE POSE ESTIMATION RESULTS ON METU-VIS<sub>TIR</sub>. SUCCESS RATE DENOTES THE RATIO OF VALID POSE EVALUATIONS OVER ALL 2590 IMAGE PAIRS, AND AUC IS OBTAINED BY COMBINING THE *cloudy-cloudy* AND *cloudy-sunny* SPLIT SCORES ACCORDING TO THE NUMBER OF SCENES IN EACH SPLIT.

Category	Method	Success Rate	AUC@5	AUC@10	AUC@20	
Sparse	SuperPoint+MINIMA-LG	0.941	<b>0.192</b>	<b>0.373</b>	<b>0.556</b>	
	SuperPoint+SuperGlue	<u>0.964</u>	<u>0.036</u>	<u>0.088</u>	<u>0.168</u>	
	SuperPoint+LightGlue	0.941	0.016	0.043	0.090	
	ALIKED+LightGlue	0.807	0.008	0.021	0.049	
	D2Net	<b>1.000</b>	0.007	0.020	0.052	
	RIFT	<b>1.000</b>	0.006	0.018	0.048	
	DeDoDe	<b>1.000</b>	0.004	0.010	0.029	
	XFeat(sparse)	<b>1.000</b>	0.003	0.010	0.033	
	XFeat+LightGlue	0.410	0.001	0.005	0.017	
	RoRD	<b>1.000</b>	0.002	0.004	0.014	
	SuperPoint+MNN	<b>1.000</b>	0.001	0.004	0.014	
	R2D2	<b>1.000</b>	0.000	0.001	0.005	
	MIFNet(XFeat)	0.299	0.000	0.001	0.005	
	SIFT	<b>1.000</b>	0.000	0.000	0.002	
	Semi-Dense	MINIMA(XoFTR)	0.997	<b>0.197</b>	<b>0.362</b>	<b>0.533</b>
		XoFTR	<b>1.000</b>	0.185	0.354	0.528
MINIMA(LoFTR)		<b>1.000</b>	0.157	0.311	0.479	
MINIMA(ELoFTR)		<b>1.000</b>	0.118	0.269	0.455	
ASpanFormer		<b>1.000</b>	0.041	0.098	0.194	
ELoFTR		<b>1.000</b>	0.038	0.096	0.201	
TopicFM		<b>1.000</b>	0.036	0.085	0.165	
LoFTR		<b>1.000</b>	0.025	0.068	0.152	
Dense		MINIMA(RoMa)	<b>1.000</b>	<b>0.379</b>	<b>0.612</b>	<b>0.786</b>
	RoMa	<b>1.000</b>	0.249	0.468	0.673	
	RoMa v2	<b>1.000</b>	0.225	0.436	0.635	
	GIM(RoMa)	<b>1.000</b>	0.165	0.374	0.594	
	MASt3R	<b>1.000</b>	0.100	0.239	0.407	
	DKM	<u>0.999</u>	0.046	0.100	0.172	
	GIM(DKM)	<b>1.000</b>	0.000	0.030	0.129	
	XFeat(dense)	<b>1.000</b>	0.003	0.009	0.030	

success rates within distance thresholds of 3 m, 5 m, and 10 m over all test pairs, denoted as SR@3m, SR@5m, and SR@10m:

$$\text{MedErr}_m = \text{median}(\{e_i\}_{i \in \mathcal{S}}) \quad (2)$$

$$\text{SR}@_\tau = \frac{1}{N} \sum_{i=1}^N \mathbf{1}(e_i \leq \tau), \quad \tau \in \{3, 5, 10\} \text{ m} \quad (3)$$

where  $\mathcal{S}$  is the set of successfully evaluated pairs and  $N$  is the total number of test pairs. Lower  $\text{MedErr}_m$  and higher  $\text{SR}@3\text{m}/\text{SR}@5\text{m}/\text{SR}@10\text{m}$  indicate better geo-localization performance and stronger robustness in practical deployment.

#### IV. EXPERIMENTS AND RESULTS

We conduct a comprehensive evaluation of 30 state-of-the-art feature matching methods under a unified implementation and metric setting. For clarity, we abbreviate LightGlue as LG. Our benchmark includes 14 sparse methods, namely ALIKED+LG [7], [17], D2Net [36], DeDoDe [37], MIFNet(XFeat) [38], [39], R2D2 [15], RIFT [5], RoRD [40], SIFT [4], SuperPoint+LG [6], [17], SuperPoint+MINIMA-LG [6], [9], [17], SuperPoint+MNN [6], SuperPoint+SuperGlue [6], [16], XFeat(sparse) [39], and XFeat+LG [17], [39]; 8 semi-dense methods, namely ASpanFormer [21], ELoFTR [20], LoFTR [19], MINIMA(ELoFTR) [9], MINIMA(LoFTR) [9],

MINIMA(XoFTR) [9], TopicFM [41], and XoFTR [8]; and 8 dense methods, namely DKM [23], GIM(DKM) [24], GIM(RoMa) [24], MASt3R [28], MINIMA(RoMa) [9], RoMa [25], RoMa v2 [26], and XFeat(dense) [39].

Note that, MINIMA [9] and XoFTR [8] are specifically designed for IR-VIS matching, while RIFT [5] represents a traditional method with cross-modal capabilities. We include MASt3R [28] instead of DUST3R due to its superior robustness in challenging scenarios.

#### A. Experimental Setup

All experiments are conducted on a workstation equipped with an NVIDIA RTX 4090 GPU. To ensure fair comparison, we standardize the implementation parameters across all methods. Images are resized to maintain a maximum dimension of 640 pixels while preserving their aspect ratio. For feature matching, we set the maximum number of matches to 2048 for all methods. When applying RANSAC for geometric verification, we use a threshold of 3.0 pixels.

For adaptive preprocessing experiments, we employ the MobileNetV4-based front-end described above to select a preprocessing branch for each input pair. The classification network operates on  $224 \times 224$  image pairs and predicts one of four candidate branches, including no preprocessing, unsharp enhancement, Scharr-gradient with local contrast normalization, and morphological-gradient enhancement. The selected preprocessing result is then passed to the downstream matcher for geometric estimation and localization.

#### B. Results and Discussion

The evaluation focuses on MSCM for homography estimation, METU-Vis<sub>TIR</sub> for relative pose estimation, and ThermoSat for geo-localization under both base and hard protocols. These results reveal clear differences among sparse, semi-dense, and dense matchers under progressively harder cross-modal geometric tasks.

1) *Homography Estimation*: For homography estimation on MSCM, Table I reports success rate together with AUC@5/10/20. Dense RoMa-family dominate performance on this task. **MINIMA(RoMa)** achieves the best overall accuracy with AUC@5/10/20 of 0.198/0.509/0.733, followed by **RoMa** (0.151/0.438/0.672) and **XoFTR** (0.136/0.414/0.640). Among sparse methods, the **SuperPoint+MINIMA-LG** baseline is strongest with AUC@5/10/20 of 0.151/0.452/0.689, surpassing **SuperPoint+SuperGlue** and **SuperPoint+LightGlue**, while handcrafted baselines such as SIFT and RIFT are far behind. **RoMa v2** attains a 1.000 success rate, while its AUC@10 of 0.257 is still below RoMa, indicating that the gap mainly comes from geometric accuracy rather than failed estimations.

2) *Relative Pose Estimation*: For relative pose estimation on METU-Vis<sub>TIR</sub>, Table II shows that **MINIMA(RoMa)** still delivers the best overall accuracy, with AUC@5/10/20 of 0.379/0.612/0.786, followed by **RoMa** (0.249/0.468/0.673) and **RoMa v2** (0.225/0.436/0.635). A notable exception appears in the sparse family: **SuperPoint+MINIMA-LG**

TABLE III  
GEO-LOCALIZATION RESULTS ON THERMOSAT. LOWER MEDERR<sub>m</sub> AND HIGHER SR@3M/SR@5M/SR@10M ARE BETTER.

Category	Method	Base				Hard				
		MedErr <sub>m</sub>	SR@3m	SR@5m	SR@10m	MedErr <sub>m</sub>	SR@3m	SR@5m	SR@10m	
Sparse	XFeat(sparse)	0.746	<b>0.786</b>	<b>0.851</b>	<b>0.921</b>	1.417	<b>0.305</b>	<b>0.349</b>	<b>0.398</b>	
	SuperPoint+MINIMA-LG	<b>0.452</b>	0.686	0.719	0.758	<b>0.470</b>	0.284	0.294	0.319	
	XFeat+LightGlue	0.663	0.660	0.714	0.779	0.764	0.243	0.254	0.278	
	SuperPoint+SuperGlue	1.355	0.529	0.590	0.665	2.748	0.226	0.245	0.298	
	SuperPoint+LightGlue	1.429	0.513	0.573	0.655	3.404	0.208	0.234	0.282	
	ALIKED+LightGlue	4.845	0.340	0.394	0.493	6.744	0.142	0.162	0.195	
	D2Net	1.766	0.602	0.690	<u>0.812</u>	10.680	0.115	0.142	0.233	
	DeDoDe	9.312	0.242	0.314	0.519	13.050	0.085	0.107	0.180	
	RIFT	1.965	0.554	0.626	0.749	14.674	0.064	0.091	0.145	
	SuperPoint+MNN	11.276	0.188	0.264	0.448	15.420	0.061	0.089	0.154	
	MIFNet(XFeat)	1.690	0.481	0.562	0.629	5.668	0.046	0.079	0.125	
	RoRD	14.972	0.102	0.160	0.308	14.988	0.023	0.050	0.119	
	R2D2	16.244	0.071	0.114	0.251	18.287	0.007	0.020	0.077	
	SIFT	18.561	0.010	0.025	0.108	17.803	0.001	0.008	0.066	
	Semi-Dense	MINIMA(LoFTR)	0.456	0.847	0.905	0.950	<u>1.201</u>	0.291	<b>0.319</b>	<b>0.383</b>
		MINIMA(ELoFTR)	<b>0.371</b>	<b>0.945</b>	<b>0.959</b>	<b>0.977</b>	<b>0.751</b>	<b>0.296</b>	0.312	0.337
ELoFTR		1.772	0.593	0.704	0.835	5.522	0.192	0.233	0.314	
LoFTR		2.343	0.540	0.612	0.763	6.788	0.173	0.215	0.294	
MINIMA(XoFTR)		0.854	0.680	0.754	0.833	4.027	0.185	0.212	0.267	
TopicFM		2.288	0.543	0.637	0.772	6.797	0.159	0.210	0.286	
XoFTR		1.528	0.582	0.671	0.793	9.174	0.153	0.188	0.252	
ASpanFormer		1.091	0.694	0.787	0.874	10.535	0.129	0.159	0.228	
Dense		MINIMA(RoMa)	<b>0.343</b>	<b>0.893</b>	<b>0.909</b>	0.917	<b>0.333</b>	<b>0.441</b>	<b>0.456</b>	<b>0.472</b>
	GIM(RoMa)	0.430	0.835	0.871	0.895	<u>0.392</u>	0.430	0.441	0.452	
	RoMa	0.446	0.810	0.855	0.892	0.421	0.368	0.383	0.415	
	XFeat(dense)	0.760	0.797	0.869	<b>0.928</b>	1.901	0.274	0.310	0.376	
	GIM(DKM)	1.814	0.560	0.613	0.706	1.592	0.285	0.306	0.350	
	DKM	1.693	0.565	0.633	0.738	4.256	0.216	0.251	0.294	
	RoMa v2	20.131	0.153	0.178	0.239	6.061	0.225	0.240	0.260	
	MASt3R	18.718	0.149	0.188	0.262	20.305	0.016	0.022	0.056	

reaches 0.192/0.373/0.556, clearly outperforming the other sparse baselines and even surpassing several semi-dense methods on this benchmark. Among the remaining semi-dense matchers, **MINIMA(XoFTR)** and **XoFTR** remain the strongest, with AUC@10 of 0.362 and 0.354, respectively.

3) *Geo-localization*: For geo-localization on ThermoSat, Table III summarizes results under both the base and hard protocols. Under the base protocol, **MINIMA(ELoFTR)** provides the highest threshold-based localization rates, reaching SR@3m/SR@5m/SR@10m of 0.945/0.959/0.977, while **MINIMA(RoMa)** yields the lowest median error of 0.343 m with SR@5m = 0.909. **GIM(RoMa)** and **RoMa** also remain highly competitive with sub-meter median errors and SR@5m above 0.85. Under the hard protocol, all methods degrade markedly, confirming the challenge introduced by the simulated attitude-angle and altitude variations. **MINIMA(RoMa)** remains the strongest method with MedErr<sub>m</sub> = 0.333 m and SR@5m = 0.456, followed by **GIM(RoMa)** (0.392 m, 0.441) and **RoMa** (0.421 m, 0.383). Among sparse methods, **XFeat(sparse)** is the most robust baseline on the hard split, but its localization accuracy still remains below that of the strongest dense methods. **RoMa v2** again underperforms RoMa on ThermoSat, especially on the base protocol, where its median error rises to 20.131 m.

4) *Impact of Adaptive Preprocessing Front-end*: Instead of applying one fixed enhancement pipeline to all samples, we evaluate the proposed MobileNetV4-based adaptive pre-

processing front-end using downstream benchmark metrics. For MSCM, we do not train the gate on the full 7083-pair benchmark directly; instead, we first sample a 2000-pair subset from MSCM and then split it into 1600 training pairs and 400 validation pairs. For METU-VisTIR, we use 1382 *cloudy-cloudy* pairs for training and 1208 *cloudy-sunny* pairs for validation. For ThermoSat, we adopt sequence-disjoint splits for both the base and hard protocols. The base protocol uses five sequences for training and two unseen sequences for testing, corresponding to 546 annotated pairs (1092 images) for training and 286 annotated pairs (572 images) for testing. The hard protocol is constructed from the corresponding ThermoSat sequences by introducing additional attitude-angle and altitude perturbations while preserving the same underlying localization scenes, yielding 539 annotated pairs (1078 images) for training and 224 annotated pairs (448 images) for testing.

Table IV reports downstream baseline-versus-adaptive comparisons without mixing in classifier-only diagnostics. On the MSCM validation split, positive gains are observed for all selected matchers, with the improvements appearing for **DKM**, **ALIKED+LightGlue**, **TopicFM**, and **LoFTR**. On METU-VisTIR, the adaptive front-end also produces consistent gains across all listed matchers, although the improvement for **MINIMA(RoMa)** is now marginal, while the largest relative gains are still observed for **ALIKED+LightGlue**, **SuperPoint+LightGlue**, **TopicFM**,

TABLE IV

ADAPTIVE PREPROCESSING RESULTS ON MSCM, METU-VIS<sub>TIR</sub>, AND THERMOSAT USING DOWNSTREAM BENCHMARK METRICS. FOR MSCM AND METU-VIS<sub>TIR</sub>, WE REPORT AUC@10 ON THE CORRESPONDING VALIDATION SPLITS. FOR THERMOSAT, WE REPORT SR@10M ON THE SEQUENCE-DISJOINT HARD TEST SPLIT. THE “GAIN (%)” ROWS DENOTE THE RELATIVE PERCENTAGE CHANGE FROM THE BASELINE TO THE ADAPTIVE RESULT. MSCM RESULTS ARE COMPUTED ON THE 400-PAIR VALIDATION SPLIT SAMPLED FROM THE 7083-PAIR BENCHMARK. METU-VIS<sub>TIR</sub> RESULTS ARE COMPUTED ON THE 1208-PAIR *cloudy-sunny* VALIDATION SPLIT.

Dataset	Setting	MINIMA(RoMa)	XoFTR	MINIMA(LoFTR)	SuperPoint+LightGlue	TopicFM	LoFTR	DKM	ALIKED+LightGlue
MSCM	Baseline	0.526	0.421	0.391	0.354	0.325	0.311	0.308	0.292
MSCM	<b>Adaptive</b>	<b>0.529</b>	<b>0.426</b>	<b>0.399</b>	<b>0.364</b>	<b>0.356</b>	<b>0.335</b>	<b>0.344</b>	<b>0.328</b>
MSCM	Gain (%)	+0.6%	+1.2%	+2.0%	+2.8%	+9.5%	+7.7%	+11.7%	+12.3%
METU-VisTIR	Baseline	0.557	0.300	0.230	0.061	0.088	0.068	0.121	0.041
METU-VisTIR	<b>Adaptive</b>	<b>0.561</b>	<b>0.312</b>	<b>0.247</b>	<b>0.098</b>	<b>0.135</b>	<b>0.100</b>	<b>0.183</b>	<b>0.088</b>
METU-VisTIR	Gain (%)	+0.7%	+4.0%	+7.4%	+60.7%	+53.4%	+47.1%	+51.2%	+114.6%
ThermoSat (Hard)	Baseline	0.478	0.281	0.393	0.286	0.299	0.286	0.304	0.174
ThermoSat (Hard)	<b>Adaptive</b>	<b>0.485</b>	<b>0.312</b>	<b>0.405</b>	<b>0.301</b>	<b>0.355</b>	<b>0.347</b>	<b>0.333</b>	<b>0.274</b>
ThermoSat (Hard)	Gain (%)	+1.5%	+11.0%	+3.1%	+5.2%	+18.7%	+21.3%	+9.5%	+57.5%

**DKM**, and **LoFTR**. For ThermoSat, we keep only the harder sequence-disjoint protocol in this table. Under this setting, **MINIMA(RoMa)** remains the strongest selected matcher after adaptation with  $SR@10m = 0.485$ , while **TopicFM**, **LoFTR**, and **ALIKED+LightGlue** still show the most notable relative gains of 18.7%, 21.3%, and 57.5%, respectively. These results are consistent with the benchmark observations in the previous subsections: preprocessing preference is strongly coupled with both the scene characteristics and the downstream matcher.

Overall, the adaptive front-end provides a practical way to exploit the fact that the preferred preprocessing branch varies across image pairs and downstream matchers. This observation is consistent with our conjecture: in IR-VIS matching, no single handcrafted preprocessing strategy is universally optimal, while lightweight learned routing can yield measurable gains without changing the matcher architecture itself.

5) *Efficiency Comparison*: Table V shows that the sparse family are the fastest methods, with **SuperPoint+MNN** and **XFeat(sparse)** providing the lowest runtime. In the semi-dense family, **MINIMA(ELoFTR)** and **ELoFTR** offer the best efficiency, while **XFeat(dense)** is the most lightweight dense method by a clear margin. In contrast, the RoMa-based dense models and **MAS<sub>t</sub>3R** provide stronger representation capacity at substantially higher computational cost.

## V. CONCLUSION

In this paper, we thoroughly test the performance of cross-modal feature algorithms between infrared and visible images. The experiments are conducted using **30** algorithms across **10** diverse cross-modal datasets. We also release ThermoSat, a self-collected infrared-satellite dataset captured by a DJI Matrice 4T platform, and evaluate practical cross-modal visual localization on this dataset. The evaluation demonstrates **MINIMA-RoMa**, **RoMa**, and **MINIMA-LG** consistently outperform other algorithms across various cross-modal scenarios and tasks. **RoMa** achieves excellent cross-modal performance by leveraging **DINOv2**’s semantic-rich features that remain consistent to modality differences, while

TABLE V  
EFFICIENCY COMPARISON AT  $640 \times 512$ .

Method	Params (M)	GFLOPs	Runtime (ms)
<i>Sparse</i>			
SuperPoint+MNN	1.301	111.350	<b>9.29</b>
XFeat(sparse)	1.545	<b>5.731</b>	17.47
SuperPoint+LightGlue	13.152	134.122	32.21
XFeat+LightGlue	1.545	26.325	37.71
ALIKED+LightGlue	12.562	47.327	38.24
SuperPoint+MINIMA-LG	13.152	134.122	32.21
SuperPoint+SuperGlue	13.324	129.415	54.10
DeDoDe	28.079	2683.537	66.66
R2D2	<b>0.484</b>	1894.098	100.53
SIFT	N/A	N/A	125.36
D2Net	7.635	724.579	188.22
RoRD	7.635	724.579	188.57
MIFNet(XFeat)	15.981	52930.926	1780.71
RIFT	N/A	N/A	3667.13
<i>Semi-Dense</i>			
MINIMA(ELoFTR)	15.054	462.301	<b>34.76</b>
ELoFTR	15.054	462.301	<b>34.76</b>
LoFTR	11.561	763.657	42.56
MINIMA(XoFTR)	<b>11.092</b>	606.850	47.47
MINIMA(LoFTR)	11.561	763.657	42.56
XoFTR	<b>11.092</b>	606.850	47.47
TopicFM	11.842	<b>461.943</b>	51.36
ASpanFormer	15.757	787.184	112.39
<i>Dense</i>			
XFeat(dense)	<b>1.545</b>	<b>21.207</b>	<b>27.54</b>
DKM	72.261	3086.218	322.71
RoMa v2	425.421	13998.896	422.70
GIM(DKM)	70.212	5265.993	452.97
RoMa	111.288	16347.327	614.60
MINIMA(RoMa)	111.288	16347.327	614.60
GIM(RoMa)	111.288	16347.327	618.61
MAS <sub>t</sub> 3R	688.639	14317.709	3761.46

**MINIMA** series enhances performance through advanced generative models for infrared data synthesis. In addition, the adaptive preprocessing front-end shows that the preferred enhancement branch varies across image pairs and downstream matchers, and that lightweight learned routing can provide consistent downstream gains on **MSCM**, **METU-Vis<sub>TIR</sub>**, and the harder **ThermoSat** protocol without modifying the matcher architecture itself. **CM-Bench** provides a reliable baseline of cross-modal feature matching and is useful for researchers to design practical cross-modality systems.

## REFERENCES

- [1] Y. Qin, L. Bruzzone, C. Gao, and B. Li, “Infrared small target detection based on facet kernel and random walker,” *IEEE Transactions on Geoscience and Remote Sensing*, vol. 57, no. 9, pp. 7104–7118, 2019.

- [2] Q. Zhao, L. Dong, M. Liu, L. Kong, X. Chu, M. Hui, and Y. Zhao, "Visible/infrared image registration based on region-adaptive contextual multifeatures," *IEEE Transactions on Geoscience and Remote Sensing*, vol. 62, pp. 1–17, 2024.
- [3] J. Jiang, X. Chen, W. Dai, Z. Gao, and Y. Zhang, "Thermal-inertial slam for the environments with challenging illumination," *IEEE Robotics and Automation Letters*, vol. 7, no. 4, pp. 8767–8774, 2022.
- [4] D. G. Lowe, "Distinctive image features from scale-invariant keypoints," *International Journal of Computer Vision*, vol. 60, pp. 91–110, 2004.
- [5] J. Li, Q. Hu, and M. Ai, "Rift: Multi-modal image matching based on radiation-variation insensitive feature transform," *IEEE Transactions on Image Processing*, vol. 29, pp. 3296–3310, 2019.
- [6] D. DeTone, T. Malisiewicz, and A. Rabinovich, "Superpoint: Self-supervised interest point detection and description," in *Proceedings of the IEEE Conference on Computer Vision and Pattern Recognition Workshops*, 2018, pp. 224–236.
- [7] X. Zhao, X. Wu, W. Chen, P. C. Chen, Q. Xu, and Z. Li, "Aliked: A lighter keypoint and descriptor extraction network via deformable transformation," *IEEE Transactions on Instrumentation and Measurement*, vol. 72, pp. 1–16, 2023.
- [8] Ö. Tuzcuoğlu, A. Köksal, B. Sofu, S. Kalkan, and A. A. Alatan, "Xoftr: Cross-modal feature matching transformer," in *Proceedings of the IEEE/CVF Conference on Computer Vision and Pattern Recognition*, 2024, pp. 4275–4286.
- [9] X. Jiang, J. Ren, Z. Li, X. Zhou, D. Liang, and X. Bai, "Minima: Modality invariant image matching," *arXiv preprint arXiv:2412.19412*, 2024.
- [10] J. Yu, H. Ye, J. Jiao, P. Tan, and H. Zhang, "Gv-bench: Benchmarking local feature matching for geometric verification of long-term loop closure detection," in *2024 IEEE/RISJ International Conference on Intelligent Robots and Systems (IROS)*. IEEE, 2024, pp. 7922–7928.
- [11] Y. Jin, D. Mishkin, A. Mishchuk, J. Matas, P. Fua, K. M. Yi, and E. Trulls, "Image matching across wide baselines: From paper to practice," *International Journal of Computer Vision*, vol. 129, no. 2, pp. 517–547, 2021.
- [12] S. Bonilla, C. Di Vece, R. Daher, X. Ju, D. Stoyanov, F. Vasconcelos, and S. Bano, "Mismatched: Evaluating the limits of image matching approaches and benchmarks," *arXiv preprint arXiv:2408.16445*, 2024.
- [13] E. Rublee, V. Rabaud, K. Konolige, and G. Bradski, "ORB: An efficient alternative to SIFT or SURF," in *2011 International Conference on Computer Vision*, 2011, pp. 2564–2571.
- [14] H. Bay, A. Ess, T. Tuytelaars, and L. Van Gool, "Speeded-up robust features (surf)," *Computer Vision and Image Understanding*, vol. 110, no. 3, pp. 346–359, 2008.
- [15] J. Revaud, C. De Souza, M. Humenberger, and P. Weinzaepfel, "R2d2: Reliable and repeatable detector and descriptor," *Advances in neural information processing systems*, vol. 32, pp. 12 405–12 415, 2019.
- [16] P.-E. Sarlin, D. DeTone, T. Malisiewicz, and A. Rabinovich, "Superglue: Learning feature matching with graph neural networks," in *Proceedings of the IEEE/CVF Conference on Computer Vision and Pattern Recognition*, 2020, pp. 4938–4947.
- [17] P. Lindenberger, P.-E. Sarlin, and M. Pollefeys, "Lightglue: Local feature matching at light speed," in *Proceedings of the IEEE/CVF International Conference on Computer Vision*, 2023, pp. 17 627–17 638.
- [18] Q. Zhou, T. Sattler, and L. Leal-Taixe, "Patch2pix: Epipolar-guided pixel-level correspondences," in *Proceedings of the IEEE/CVF Conference on Computer Vision and Pattern Recognition*, 2021, pp. 4669–4678.
- [19] J. Sun, Z. Shen, Y. Wang, H. Bao, and X. Zhou, "Loftr: Detector-free local feature matching with transformers," in *Proceedings of the IEEE/CVF Conference on Computer Vision and Pattern Recognition*, 2021, pp. 8922–8931.
- [20] Y. Wang, X. He, S. Peng, D. Tan, and X. Zhou, "Efficient loftr: Semi-dense local feature matching with sparse-like speed," in *Proceedings of the IEEE/CVF Conference on Computer Vision and Pattern Recognition*, 2024, pp. 21 666–21 675.
- [21] H. Chen, Z. Luo, L. Zhou, Y. Tian, M. Zhen, T. Fang, D. Mckinnon, Y. Tsin, and L. Quan, "Aspanformer: Detector-free image matching with adaptive span transformer," in *European Conference on Computer Vision*. Springer, 2022, pp. 20–36.
- [22] Q. Wang, J. Zhang, K. Yang, K. Peng, and R. Stiefelwagen, "Match-former: Interleaving attention in transformers for feature matching," in *Proceedings of the Asian Conference on Computer Vision*, 2022, pp. 2746–2762.
- [23] J. Edstedt, I. Athanasiadis, M. Wadenbäck, and M. Felsberg, "Dkm: Dense kernelized feature matching for geometry estimation," in *Proceedings of the IEEE/CVF Conference on Computer Vision and Pattern Recognition*, 2023, pp. 17 765–17 775.
- [24] X. Shen, Z. Cai, W. Yin, M. Müller, Z. Li, K. Wang, X. Chen, and C. Wang, "Gim: Learning generalizable image matcher from internet videos," *arXiv preprint arXiv:2402.11095*, 2024.
- [25] J. Edstedt, Q. Sun, G. Bökman, M. Wadenbäck, and M. Felsberg, "Roma: Robust dense feature matching," in *Proceedings of the IEEE/CVF Conference on Computer Vision and Pattern Recognition*, 2024, pp. 19 790–19 800.
- [26] J. Edstedt, D. Nordström, Y. Zhang, G. Bökman, J. Astermark, V. Larsson, A. Heyden, F. Kahl, M. Wadenbäck, and M. Felsberg, "Roma v2: Harder better faster denser feature matching," *arXiv preprint arXiv:2511.15706*, 2025.
- [27] S. Wang, V. Leroy, Y. Cabon, B. Chidlovskii, and J. Revaud, "Dust3r: Geometric 3d vision made easy," in *Proceedings of the IEEE/CVF Conference on Computer Vision and Pattern Recognition*, 2024, pp. 20 697–20 709.
- [28] V. Leroy, Y. Cabon, and J. Revaud, "Grounding image matching in 3d with mast3r," in *European Conference on Computer Vision*. Springer, 2025, pp. 71–91.
- [29] P. Zhang, J. Zhao, D. Wang, H. Lu, and X. Ruan, "Visible-thermal uav tracking: A large-scale benchmark and new baseline," in *Proceedings of the IEEE/CVF Conference on Computer Vision and Pattern Recognition*, 2022, pp. 8886–8895.
- [30] X. Jia, C. Zhu, M. Li, W. Tang, and W. Zhou, "Llvp: A visible-infrared paired dataset for low-light vision," in *Proceedings of the IEEE/CVF International Conference on Computer Vision*, 2021, pp. 3496–3504.
- [31] J. Liu, X. Fan, Z. Huang, G. Wu, R. Liu, W. Zhong, and Z. Luo, "Target-aware dual adversarial learning and a multi-scenario multi-modality benchmark to fuse infrared and visible for object detection," in *Proceedings of the IEEE/CVF Conference on Computer Vision and Pattern Recognition*, 2022, pp. 5802–5811.
- [32] J. Ma, L. Tang, F. Fan, J. Huang, X. Mei, and Y. Ma, "Swinfusion: Cross-domain long-range learning for general image fusion via swin transformer," *IEEE/CAA Journal of Automatica Sinica*, vol. 9, no. 7, pp. 1200–1217, 2022.
- [33] S. Hwang, J. Park, N. Kim, Y. Choi, and I. So Kweon, "Multispectral pedestrian detection: Benchmark dataset and baseline," in *Proceedings of the IEEE conference on Computer Vision and Pattern Recognition*, 2015, pp. 1037–1045.
- [34] FLIR Systems, Inc., "Flir adas dataset," <https://www.flir.com/oem/adas/adas-dataset-form/>, 2018, accessed: 2026-03-08.
- [35] K. G. Derpanis, "Overview of the ransac algorithm," *Image Rochester NY*, vol. 4, no. 1, pp. 2–3, 2010.
- [36] M. Dusmanu, I. Rocco, T. Pajdla, M. Pollefeys, J. Sivic, A. Torii, and T. Sattler, "D2-net: A trainable cnn for joint description and detection of local features," in *Proceedings of the IEEE/CVF Conference on Computer Vision and Pattern Recognition*, 2019, pp. 8092–8101.
- [37] J. Edstedt, G. Bökman, M. Wadenbäck, and M. Felsberg, "Dedode: Detect, don't describe—describe, don't detect for local feature matching," in *2024 International Conference on 3D Vision (3DV)*, 2024, pp. 148–157.
- [38] Y. Liu, Z. Sun, B. Yu, Y. Zhao, B. Du, Y. Xu, and J. Cheng, "Mifnet: Learning modality-invariant features for generalizable multimodal image matching," *IEEE transactions on image processing*, vol. 34, pp. 3593–3608, 2025.
- [39] G. Potje, F. Cadar, A. Araujo, R. Martins, and E. R. Nascimento, "Xfeat: Accelerated features for lightweight image matching," in *2024 IEEE/CVF Conference on Computer Vision and Pattern Recognition (CVPR)*, 2024, pp. 2682–2691.
- [40] U. S. Parihar, A. Gujarathi, K. Mehta, S. Tourani, S. Garg, M. Milford, and K. M. Krishna, "Rord: Rotation-robust descriptors and orthographic views for local feature matching," in *2021 IEEE/RISJ International Conference on Intelligent Robots and Systems (IROS)*, 2021, pp. 1593–1600.
- [41] K. T. Giang, S. Song, and S. Jo, "Topicfm: Robust and interpretable topic-assisted feature matching," in *Proceedings of the AAAI Conference on Artificial Intelligence*, vol. 37, no. 2, 2023, pp. 2447–2455.